CrystEngComm

Accepted Manuscript

ROYAL SOCIETY OF CHEMISTRY

www.rsc.org/crystengcomm

Cite this: DOI: 10.1039/c0xx00000x

www.rsc.org/xxxxxx

ARTICLE TYPE

Fluorinated mixed valence Fe(II)-Fe(III) phosphites with channels templated by linear tetramine chains. Structural and magnetic implications of partial replacement of Fe(II) by Co(II)

Joseba Orive,[a] Roberto Fernández de Luis,[a] Jesús Rodríguez Fernández,[b] Estibaliz Legarra,[c] Fernando Plazaola,[c] María I. Arriortua[a,*]

Received (in XXX, XXX) Xth XXXXXXXXX 20XX, Accepted Xth XXXXXXXXX 20XX
DOI: 10.1039/b000000x

Three new fluorinated mixed valence Fe(II)-Fe(III) phosphites were synthesized employing mild hydrothermal conditions. $(H_4baepn)_{0.5}[Fe^{III}_{2.3}Fe^{II}_{1.7}(H_2O)_2(HPO_3)_{4-(x+y)}(HPO_4)_x(PO_4)_yF_4]$ (x≃0.13, y≃0.3) **1** (baepn = N,N'-Bis(2-aminoethyl)-1,3-propanediamine ($C_7N_4H_{20}$)) and the Co(II)-substituted phase with formula $(H_4baepn)_{0.5}[Fe^{III}_{2.0}Fe^{II}_{0.71}Co^{II}_{1.29}(H_2O)_2(HPO_3)_{4-x}(HPO_4)_xF_4]$ (x≃0.38) **2** were studied by single crystal X-ray diffraction. The phase with the major content of Co(II), $(H_4baepn)_{0.5}[Fe^{III}_{2.0}Fe^{II}_{0.62}Co^{II}_{1.38}(H_2O)_2(HPO_3)_{4-x}(HPO_4)_xF_4]$ (x≃0.38) **3** was achieved as polycrystalline powder and studied by Rietveld refinement by using the structural model of **2**. These compounds have been characterized by ICP-Q-MS, thermogravimetric and thermodiffractometric analyses, and XPS, IR, UV/vis and Mössbauer spectroscopies. Single crystal data indicate that phases **1** and **2** crystallize in the $P2_1/c$ space group with lattice parameters: a= 13.6808(4), b= 12.6340(2), c= 12.7830(3) Å and β = 116.983(4)º for **1** and a= 13.6823(4), b= 12.6063(3), c= 12.7535(4) Å and β = 116.988(4)º for **2**, with Z= 4. Reciprocal space of **1** shows satellite reflections with a modulation wavevector q = 0.284(2)a* which indicate an incommensurate long-range order. The average structure of these compounds is built up by a 3D lattice constructed by inorganic layers of Fe(III) chains and Fe(II), Co(II) dimers joined by phosphite groups partially substituted by HPO_4 and PO_4 tetrahedral groups. These anionic layers stack along the [100] direction encapsulating linear tetramines into eight-membered open channels involving host–guest interaction. Magnetic measurements of **1** and **3** show an antiferromagnetic coupling as the major interactions, exhibiting a weak ferromagnetic component together with a spin glass transition at low temperature in case of **1**. Heat capacity measurements show a small anomaly at 20.5 K for **1** and a sharp magnetic peak at 28 K for **3**. Unexpectedly, the small anomaly observed in **1** grows with the magnetic field and becomes better defined.

Introduction

One of the challenges to be faced in the field of open framework materials science and technology is the design and the obtaining of porous compounds which combine the classical properties of the zeolites with physicochemical properties such as magnetic, optical or conductive, arising from the introduction of transition metals in the crystalline structures.[1,2]

Synthesis of microporous materials such as zeolites, alumino-silicates and phosphates or other zeotypes, which receive interest because of their potential industrial applications as solid acid catalysts, ion exchangers or in the separation of gases[2,3], is driven sometimes by using protonated amines as templates or structure directing agents (SDAs).[4]

By employing small organic amines as structure-directing agents, such as n-propylamine, n-butylamine, cyclopentylamine and cyclohexylamine extra-large-micropore compounds, for instance 16 and 18-membered-ring fluorinated gallium phosphates,[5] 16-ring channels vanadium(III) phosphites[6] and 24-ring channels zinc phosphites[7] have been hydrothermally achieved. The crystallization of them is given by a cooperative templating mechanism of multiple organic cations which reside within the voids with their hydrophobic groups pointing toward the center of the pores and the hydrophilic NH_3^+ ends interacting via hydrogen bonding with the host.

The assembly of small organic amines and their effect as SDA to direct the crystallization of large micropore aluminophosphites, zincophosphates, and aluminophosphates has also been investigated. The authors conclude that the aggregation of 1,6-hexanediamine (HDA) molecules gives rise to the formation of lamellar structures, while microporous 3D frameworks are formed mainly from the host–guest interaction between inorganic frameworks and individual 1,6-HDA.[8]

Recently, some gallium zincophosphites, NTHU-13, with channel expansion from 24-ring to 72-ring were successfully achieved by using heterometal centers and a series of aliphatic monoamines increasing the template from 4-carbon (4C)

containing butylamine to 18C octadecylamine.[9]

According to the host guest charge matching concept a highly charged inorganic framework should be templated by highly charged organic amines such as multiamines.[10] For instance, the chain-type polyamines such as TETA (10-atom-skeleton tetramine)[11], AE-DAP (8-atom-skeleton triamine)[12] and 1,6-HDA (8-atom-skeleton diamine)[13] conducted to the crystallization of $(C_6H_{22}N_4)_{0.5}[Zn_3(HPO_4)(PO_4)_2]$ (16R-channel structure with 25.6% non framework space (NFS)), $(C_5H_{18}N_3)_{0.5}[Zn_3(HPO_4)_3(PO_4)]$ (16R-channel structure with 36.2% NFS) and $(C_6H_{18}N_2)[Zn_4(PO_4)_2(HPO_4)_2]\cdot 3H_2O$ (20R-channel structure with 45.7% NFS) respectively. The role of such templates indicated that the size effect of a polyamine template is reduced with increasing number of amino groups and that NFS in the structures increases in proportion to the channel size. However, W-M. Chang *et al.* observed opposite template effects for the synthesis of zinc phosphates with 16R channel structures by using linear triamine and pentamine molecules. They concluded that the NFS is substantially augmented with increasing length and amino groups in the template.[14]

Even today the specific templating role of the SDAs is not clear. In fact, the 'true' templating effect referring to a direct correlation between the van der Waals shape of the organic template and the channel space of the resultant inorganic framework is not very usual.[15] In that regard, computer modeling has demonstrated to be a useful tool for examining nonbonding interaction energies of different host-guest systems.[16]

In spite of the scientific community has made progress in the rational organic SDAs-mediated synthesis of zeolitic inorganic open framework materials,[4] the complex chemical reaction mechanisms in which the inorganic buildings nucleate around the organic cationic species are still poorly understood. Actually, there are many examples in which the SDAs represent the products of the initial organic precursors transformed during the hydrothermal synthesis by means of hydrolysis of linear polyamines,[17] decomposition of amides[18] or N-alkylation reactions.[19] Therefore, because of the large number of parameters involved in the reaction processes still make the rational approach to the synthesis of these materials a challenging task, the "trial-and-error" strategy becomes necessary to explore new architectures when new organic templates are being used.

On the other hand, the totally or partially replacement of the classical four-coordinated PO_4^{3-} building units by 3-connected groups such as the pseudo-pyramidal HPO_3^{2-} blocks, gives rise to different connectivity patterns which can favor the construction of open structures with novel topologies and lower framework densities.[20] Moreover, the networks containing transition metal ions with open *d* shells turn out to be attractive due to their potential magnetic properties. More specifically, mixed-valent iron-containing compounds may exhibit interesting magnetic behaviour such as ferrimagnetism,[21] spin glass state[22,23] or spin canted antiferromagnetism.[24] In particular, literature refers to the existence of two examples of mixed-valent iron purely inorganic phosphites, $Li_{1.43}[Fe^{II}_{4.43}Fe^{III}_{0.57}(HPO_3)_6]\cdot 1.5H_2O$[23] and $Fe^{II}_{2.08}Fe^{III}_{0.42}(H_2O)_2(HPO_3)_{1.58}(PO_4)_{0.42}F$,[25] and three examples of mixed-valent iron organically templated phosphites, $(NH_4)[Fe_2^{II}Fe^{III}(HPO_3)_4]$,[26] $(C_4H_{12}N_2)[Fe^{II}Fe^{III}(HPO_3)_2F_3]$[27] and $(C_4N_2H_{12})[Fe^{II}_{0.86}Fe^{III}_{1.14}(HPO_3)_{1.39}(HPO_4)_{0.47}(PO_4)_{0.14}F_3]$.[28]

In addition, many times the design and synthesis of magnetic materials pass through the study of replacing the transition metals. For example, cobalt-iron bimetallic molecular magnets based on cyano-bridged coordination polymers[29] (Prussian Blue analogues) and oxalate-bridged complexes,[30] have been of great interest due to their functional magnetic properties, such as photoinduced magnetism,[31] anisotropic photoinduced magnetism in thin films,[32] and a charge-transfer-induced spin transition.[33]

In this work, in order to satisfy the host guest charge matching principle,[10] the choice of the chain-type tetramine N,N'-Bis(2-aminoethyl)-1,3-propanediamine (baepn = $C_7N_4H_{20}$) as the structure directing agent, which may arise highly charged, is accompanied by introducing F^- anion which also plays the role of template stabilizing the construction of the resulting network. While this molecule has been used for the construction of some transition metal coordination polymers,[34] wherein the organic ligand is coordinated by its four nitrogen atoms to the equatorial plane of the metallic polyhedra, we ignore its use for the synthesis of zeotypes or related compounds.

In this paper, we report on the hydrothermal synthesis, crystal structure determination, as well as the thermal, spectroscopic behaviour and magnetic properties of $(H_4baepn)_{0.5}[Fe^{III}_{2.3}Fe^{II}_{1.7}(H_2O)_2(HPO_3)_{4-(x+y)}(HPO_4)_x(PO_4)_yF_4]$ ($x\simeq 0.13$, $y\simeq 0.3$) **1**. The partially replacement of Fe(II) by Co(II) has given rise to $(H_4baepn)_{0.5}[Fe^{III}_{2.0}Fe^{II}_{0.71}Co^{II}_{1.29}(H_2O)_2(HPO_3)_{4-x}(HPO_4)_xF_4]$ ($x\simeq 0.38$) **2** as single crystals and $(H_4baepn)_{0.5}[Fe^{III}_{2.0}Fe^{II}_{0.62}Co^{II}_{1.38}(H_2O)_2(HPO_3)_{4-x}(HPO_4)_xF_4]$ ($x\simeq 0.38$) **3** as polycrystalline sample. The structural influence of the introduction of Co(II) ions by means of the analysis of the crystal structures of **1** and **2** will be discussed. Moreover, the differences in the magnetic properties between **1** and the phase with the major content of cobalt achieved, **3**, will be analyzed.

Experimental section

Synthesis and characterization

Compounds **1**, **2** and **3** were obtained as pure phases from different reactions. The synthetic procedure consists of dissolving a mixture of H_3PO_3 (7.5 mmol) and the metal salts ($FeCl_3$, 0.45 mmol for **1**; $FeCl_3$:$CoCl_2$, 0.3:0.3 mmol for **2** and $FeCl_3$:$CoCl_2$, 0.525:0.525 mmol for **3**) in 30 ml of distilled water. Then, 0.5 ml (13.9 mmol) of HF was added to the resulting solution and finally the pH was increased up to approximately 2.5 by adding dropwise the organic molecule N,N'-Bis(2-aminoethyl)-1,3-propanediamine ($C_7N_4H_{20}$). The reaction mixtures were sealed in a PTFE-lined stainless steel pressure vessel (fill factor 65%) and heated for 4 days at 170 ºC. After the reaction, black tabular single crystals of **1** and purplish products as prismatic single crystals and as powder for **2** and **3** respectively were obtained. The yield for the three compounds is around 50-60% (based on the reagent iron). The existence of Co in the samples was confirmed by XRF as preliminary characterization test.

After many attempts, compound **2** represents the phase as single crystal with the higher cobalt content achieved. The obtaining of compound **3** reveals that it is possible to achieve higher cobalt contents as powder sample. However any attempt to increase the cobalt content of the $FeCl_3$:$CoCl_2$ molar ratio provoked the crystallization of the purely inorganic fluorinated

Cite this: DOI: 10.1039/c0xx00000x

www.rsc.org/xxxxxx

ARTICLE TYPE

Co(II) phosphite $Co_{2.5}(H_2O)_2(HPO_3)_2F$[25] as impurity.

Several attempts to replace the organic template by mobile cations such as Li^+ or Na^+ were made in order to obtain a new phase with conductive properties. However, hydroxides used as lithium and/or sodium sources seemed to act merely basifying the dissolution and causing the decomposition of the organic molecule in such a way that iron(III) phosphite $(C_4N_3H_{14})[Fe_3(HPO_3)_4F_2(H_2O)_2]$[35] crystallizes.

The metal ion and phosphorous contents were confirmed by inductively coupled plasma quadrupole mass spectrometry (ICP-Q-MS) analysis, performed with a Thermo Scientific XSERIES 2 spectrometer. The amount of the fluoride anion was calculated by using a selective electrode and the amounts of C, N and H by elemental analysis. $(H_4baepn)_{0.5}[Fe^{III}_{2.3}Fe^{II}_{1.7}(H_2O)_2(HPO_3)_{4-(x+y)}(HPO_4)_x(PO_4)_yF_4]$ (x≃0.13, y≃0.3) **1**. Calculated (%): Fe, 30.02; P, 16.65; F, 10.21; C, 5.65; N, 3.77; H, 2.67. Found (%): Fe, 29.7(4); P, 16.4(3); F, 9.8(3); C 5.4(4); N, 3.5(2); H, 2.6(1). $(H_4baepn)_{0.5}[Fe^{III}_{2.0}Fe^{II}_{0.71}Co^{II}_{1.29}(H_2O)_2(HPO_3)_{4-x}(HPO_4)_xF_4]$ (x≃0.38) **2**. Calculated (%): Fe, 20.25; Co, 10.17; P, 16.57; F, 10.17; C, 5.62; N, 3.75; H, 2.70. Found (%): Fe, 20.3(3); Co, 10.2(3); P, 16.8(3); F, 10.0(3); C 5.7(4); N, 3.6(2); H, 2.7(1). $(H_4baepn)_{0.5}[Fe^{III}_{2.0}Fe^{II}_{0.62}Co^{II}_{1.38}(H_2O)_2(HPO_3)_{4-x}(HPO_4)_xF_4]$ (x≃0.38) **3**. Calculated (%): Fe, 19.57; Co, 10.88; P, 16.57; F, 10.16; C, 5.62; N, 3.75; H, 2.70. Found (%): Fe, 19.6(3); Co, 10.9(3); P, 16.7(3); F, 10.3(3); C 5.5(4); N, 3.8(2); H, 2.7(1). The densities of the three phases were measured by flotation using a mixture of CH_2I_2 and $CHCl_3$, being 2.50(3) g.cm^{-3} for **1**, 2.51(3) g.cm^{-3} for **2**, and 2.51(2) g.cm^{-3} for **3**.

Single crystal X-ray diffraction study

High quality single crystals for **1** and **2** were selected under a polarizing microscope and mounted on a glass fiber. Intensity data were collected at 100 K on an AGILENT SUPERNOVA diffractometer using a CCD (Eos) detector. Data frames were processed (unit cell determination, intensity data integration, correction for Lorentz and polarization effects,[36] and analytical absorption correction[37] taking into account the size and shape of the crystals) using the corresponding diffractometer software package.[38]

Reciprocal space analysis of compound **1** revealed the presence of weak reflections not arbitrary distributed but equidistant from the main reflections along the a* axis (Fig. S1). These additional less intense peaks, referred to as satellite reflections, are the result of the existence of a structural modulation periodic in nature, which describes a long-range order. The modulation wavevector which describe the first-order satellites with respect to the main reflections is q = 0.284(2)a* (Fig. 1), allowing the indexing of the diffraction pattern with four indices hklm. However, the low intensity of the satellite reflections together with the existence of diffuse scattering (Fig. S2) hinder the superspace group and the atomic modulation functions determination in order to describe the incommensurately modulated superstructure. While satellite reflections mark an incommensurate long-range order, diffuse scattering processes suggest the existence of a certain disorder, dynamic or static, that breaks slightly the crystallographic order. On the other hand, compound **2** shows neither satellites nor diffuse scattering (Fig. 1 and Fig. S2).

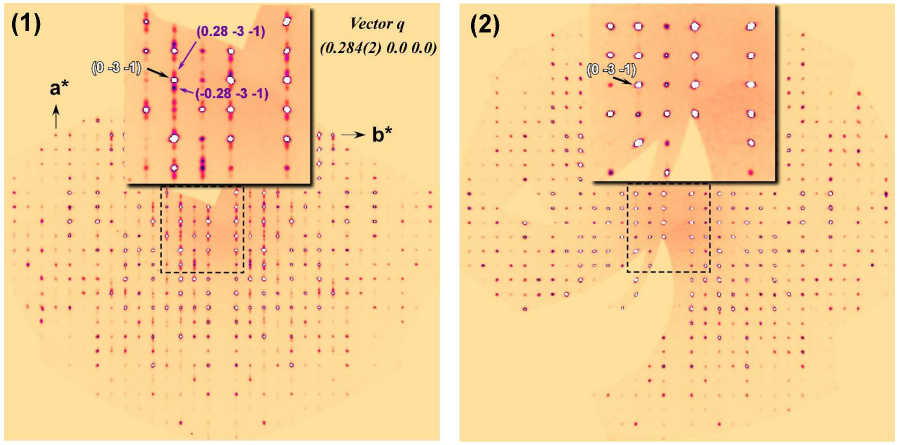

Fig. 1 Experimental images of the hk-1 layers of the diffraction patterns for **1** and **2** reconstructed using the CrysAlisPro software package.[38]

Therefore, we focused on the average structures, ignoring the satellite reflections. The structures were solved by direct methods, SHELXS 97 computer program,[39] in the monoclinic space group $P2_1/c$, and then refined by the full matrix least-squares procedure based on F^2, using the SHELXL 97 computer program[40] belonging to the WINGX software package.[41] This procedure allowed us to find the positions of the iron and phosphorous atoms, and all the other non-hydrogen atoms (F, O, C and N) were placed from subsequent Fourier-difference map calculations.

For both compounds, half organic molecule is located in the asymmetric unit and a symmetry centre generates the other half

causing a symmetry disorder of the C(4) atom with an occupation factor of 0.5, giving rise to the existence of two conformers (A and B). Due to this peculiarity, an hydrogen disorder system was modeled for their parent C(3) atom, which is bonded to C(4) (Fig. S3). Isotropic thermal displacements were used for carbon and nitrogen atoms.

From subsequent Fourier-difference map calculations, electron-densities exceeding 1.0 $e^{-}\cdot Å^{-3}$ and too long P-Q distances for apical hydrogen were observed near P(1), P(2) and P(3). The presence of both phosphite and phosphate groups was considered in these phosphorus sites. The existence of hydrogenphosphate groups, $(HPO_4)^{2-}$, were deduced from electroneutrality requirements. Hydrogen and oxygen atoms implicated in the anionic phosphorous groups replacements were treated as disordered ones with complementary occupation factors. In order to model correctly the disorder systems, P-H (1.30(1) Å) and P-O (1.50(1) Å) bonds were restrained to the ideal values. Moreover, in order to maintain the geometry of the $(HPO_3)^{2-}$ groups, the three distances of the apical hydrogen atoms to their corresponding oxygen atoms forming the pseudotetrahedra base were refined as a variable.

For compound **2**, Co^{2+} ions should be located in the M(3) and M(4) sites given the metal-ligand distances. The best fit provides a full occupation of the M(4) position and an occupation factor of 0.3(1) for M(3) in good agreement with the chemical analysis.

For the final refinement of compounds **1** and **2**, the hydrogen atoms related to the coordinated water molecules were first located and placed in geometrically ideal positions (O-H: 0.82(1) Å; H-H: 1.35(2) Å) and refined using the riding mode. Anisotropic thermal parameters were used for all the atoms belonging to the inorganic framework except for the hydrogen atoms and, the oxygen atoms implicated in the P(1), P(2) and P(3) disorder systems.

After the refinement of both phases, two residual density maxima of approximately ±3 $e^{-}\cdot Å^{-3}$ are located near N(2). In compound **2**, there are also another five peaks located along the chain suggesting positional disorder of the organic template. Furthermore, in compound **1** two electron density peaks of ±3.4 and 3.2 $e^{-}\cdot Å^{-3}$ are found at the equatorial plane of the iron $[M(4)O_2F_2(H_2O)_2]$ octahedron as well as a peak of around ±2.3 $e^{-}\cdot Å^{-3}$ at 1 Å from the P(4) atom. Such peaks located in the inorganic skeleton of **1** are also located in compound **2** but with significantly lower density values, around ±1 $e^{-}\cdot Å^{-3}$. In case of compound **1**, such anomalies are caused by the average structure resolution neglecting the satellite intensity due to the periodic character of the modulation.

Details of crystal data, data measurement and reduction, structure solution and refinement of the phases **1** and **2** are reported in Table 1. The selected bond distances and angles are reported in ESI, Tables S1 and S2. Structure drawings were made using the ATOMS 6.2,[42] VESTA 3.1.7[42] and TOPOS 4.0 programs.[43]

Powder X-ray diffraction

X-ray powder diffraction for qualitative phase analysis of phase **3** using the Rietveld method with the FullProf program[44] was recorded using a Bruker D8 Advance Vario powder diffractometer equipped with a Cu tube, Ge(111) incident beam monochromator (Cu-$K_{\alpha1}$ = 1.5406 Å), and a Sol-X energy dispersive detector. The sample was mounted on a zero background silicon wafer embedded in a generic sample holder. Data were collected from 8 to 80° 2θ (step size = 0.02º and time per step = 90 s) at RT. Fixed divergence and antiscattering slit giving a constant volume of sample illumination were used.

For the Rietveld refinement of **3**, obtained as powdered sample, the structural model of **2** was used. The cobalt content was fixed to the amount calculated by the ICP-Q-MS analysis. The fitting of the profile parameters followed by refinement of the atomic coordinates and the atomic displacement parameters of the inorganic skeleton was performed. The organic template was not refined. Four different isotropic displacement parameters were refined: one for the iron and cobalt atoms, and the remainder for de phosphorous, oxygen and fluorine atoms. Some soft constraints were included to have a chemically correct structural model.

Table 1 Crystallographic data and structure refinement parameters for phases **1** and **2** obtained by single crystal X-ray diffraction

Phase	***1***	***2***
Molecular weight ($gmol^{-1}$)	744.05	747.53
Space group	$P2_1/c$	
a, b, c (Å)	13.6808(4) 12.6340(2) 12.7830(3)	13.6823(4) 12.6063(3) 12.7535(4)
β(º)	116.983(4)	116.988(4)
V ($Å^3$), Z	1968.94(8), 4	1960.21(10), 4
ρ_{obs}, ρ_{calc} (gcm^{-3})	2.50(3), 2.51	2.51(3), 2.53
Cristal size (mm)	0.231 x 0.094 x 0.052	0.224 x 0.066 x 0.061
F(000)	1482	1480
Diffractometer / Temperature (K)	AGILENT SUPERNOVA (omega scan mode) 100(2)	
μ (mm^{-1}) Tmin./Tmáx.	3.325, 0.694/0.865	3.499, 0.757/0.839
Radiation (Å)	λ(Mo Kα) = 0.71073	
Limiting indices h, k, l	$-16\leq h\leq 15$ $k \pm 15$ $l \pm 15$	$h \pm 16$ $k \pm 15$ $l \pm 15$
Theta range (°) Completeness (%)	1.67 - 25.68, 99.8	1.67 - 25.68, 99.3
N. reflections (measured) (independents) (observed)	13887 / 3726/ 3670	13695 / 3700 / 3537
R (int) / R(sigma)	0.0189 / 0.016	0.0247 / 0.0212
Parameters Restrictions	314 / 61	317 / 51
R [I>2σ(I)]	R1= 0.0867 wR2= 0.2067	R1= 0.0658 wR2= 0.1384
R [all data]	R1= 0.0873 wR2= 0.2069	R1= 0.0676 wR2= 0.1391
Weight factor	x = 0.0577 y = 95.4386	x = 0.0072 y = 62.0640
G. O. F	1.123	1.129
Max. and Min. e. density ($eÅ^{-3}$)	3.423, -1.658	3.08, -1.619

Finally, all parameters (profile and structural) were refined simultaneously to obtain correct e.s.d.´s, obtaining a good agreement between the experimental and the calculated

diffractogram (Fig. S4). So, the proposed chemical formula for **3** is $(H_4baepn)_{0.5}[Fe^{III}_{2.0}Fe^{II}_{0.62}Co^{II}_{1.38}(H_2O)_2(HPO_3)_{4-x}(HPO_4)_xF_4]$ (x≃0.38), confirming the isostructurality between the three phases. (See Tables S3 to S5 for atomic coordinates and bond distances and angles of the Rietveld refinement of **3**).

In addition, the pattern matching analysis of the diffraction patterns of the three compounds confirming the purity of the samples is given as Supplementary Material (Fig. S5).

Physicochemical characterization techniques

Thermogravimetric analyses were performed on a SDT 2960 simultaneous DSC-TGA TA instrument for **1** and on a Netzsch STA 449C one for **2** and **3**. Alumina crucibles containing around 20 mg of every sample were heated in air at a rate of 5 °C/min from room temperature to 800 °C. Temperature dependence X-ray diffraction experiments for **1** and **3** were carried out in air with a Bruker D8 Advance diffractometer (Cu Kα radiation) equipped with, a variable-temperature stage (HTK2000), a Pt sample heater and a Vantec high-speed one dimensional detector with six degrees of angular aperture. The powder patterns were recorded in the 8≤2θ≤38º range (step size = 0.033º and time per step = 0.4 s) at intervals of 15 ºC, increasing the temperature at 10 ºCmin^{-1} from room temperature to 810 ºC. The IR spectra (KBr pellets) were obtained with a JASCO FT/IR-6100 spectrophotometer in the 400-4000 cm^{-1} range. Diffuse reflectance spectra were registered at room temperature on a Varian Cary 5000 spectrophotometer in the 200-2500 nm range. X-ray photoelectron spectra for **1**, **2** and **3** were acquired with a SPECS (Berlin, Germany) system equipped with a Phoibos 150 1D-DLD analyzer and monochromatic AlKα radiation (1486.6 eV, 300 W, 13 kV), with a multi-channel detector. Spectra were recorded in the constant pass energy mode at 80 eV for survey spectra and 30 eV for high resolution spectra, with an electron take-off angle of 90º. The spectrometer was previously calibrated using the Ag $3d_{5/2}$ line at 368.28 eV. The binding energy of the adventitious carbon (C1s) was set at 284.6 eV to correct sample charging. The spectra were fitted with the CasaXPS 2.3.16 software, which models the Gauss-Lorentzian contributions, after background subtraction (Shirley). Mössbauer spectra of **1**, **2** and **3** were obtained using a constant-acceleration Mössbauer spectrometer with a ^{57}Co/Rh source. Velocity calibration was done using a metallic Fe foil, and the Mössbauer spectral parameters are given relative to this standard at room temperature. The Mössbauer spectra were fitted with the NORMOS program.[45] Magnetic measurements on the powdered samples were performed in the temperature range 2.0-300 K for **1** and **3**, at 0.05, 0.2 and 1 T using a MPMS-7T SQUID magnetometer and a PPMS-system both from Quantum Design. Heat capacity measurements for **1** and **3** were carried out by a standard two-τ relaxation method, using a PPMS-system, with magnetic fields up to 9 T and temperatures down to 2 K.

Results and discussion

Structure description

The asymmetric unit of **1** contains 35 non-hydrogen atoms, 29 of which belong to the host framework (four Fe, four P, four F and seventeen O) and the remaining 6 to the guest species (two N and four C). Three of the oxygen atoms (O1´, O2´ and O3´) present partial occupation as they belong to the hydrogenphosphate or phosphate groups which partially replace the phosphite units. All of crystallographically independent atoms occupy general positions except the C(4) atom which present half site occupancy in order to generate the whole organic template. In **2** a total replacement of Fe(4) by Co(4) and a partial substitution of Fe(3) by Co(3) occurs in the M(3) and M(4) positions (Fig. S6).

The average structure of compound **1** is constituted by a three-dimensional lattice formed by inorganic layers of iron (III) and iron (II) octahedra joined by the P(1) and P(2) phosphite groups (Fig. 2a).

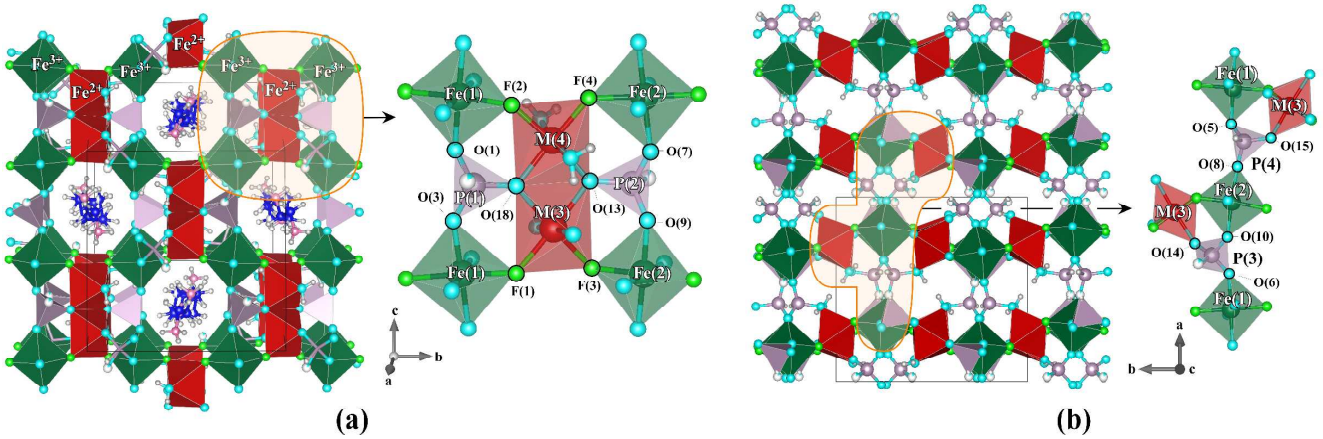

Fig. 2 a) Polyhedral representation of the 3D crystal structure of **1** viewed along the [100] direction. The shaded area shows a zoomed cut of the connectivity inside the inorganic layers. b) Layers stacking by P(3) and P(4) bridging units.

These layers link between them through the P(3) and P(4) bridging HPO_3 units (Fig. 2b). The iron (III) octahedra $Fe(1)O_4F_2$ and $Fe(2)O_4F_2$ share oxygen vertices of the phosphorous pseudotetrahedra giving rise to [001] chains. These chains are joined along the [010] direction, through the iron(II) octahedra dimers $M(3)O_4F_2$ and $M(4)O_2(H_2O)_2F_2$, which share the O(18)-O(13) edges, leading to the layers, which have eight-membered structural windows (Fig. 2a). These anionic layers stack along the [100] direction generating the open channels along the same direction, where the protonated templates are placed

longitudinally (Fig. 2a and 3a), neutralizing the negative charge excess and stabilizing the inorganic building through hydrogen bonds (Fig. 3b).

The two types of iron (III) octahedra chains, formed by the $[Fe(1)O_4F_2]$ octahedra linked together by the P(1) polyhedra and the $[Fe(2)O_4F_2]$ octahedra linked by the P(2) polyhedra, alternate in the [010] direction . Notice that the direction of the P(1)-H(1) and P(2)-H(2) bonds are opposite. Moreover, it can be observed that the octahedra are linked between them through fluorine atoms along the *b* axis giving rise to an infinite $-Fe^{3+}-F-Fe^{2+}-F-$ linkage (Fig. 2a). The $M(4)O_2(H_2O)_2F_2$ octahedron is not involved in the layers stacking because of the two water molecules are coordinated at the apical positions roughly parallel to the stacking direction.

In the $[Fe(1)O_4F_2]$ and $[Fe(2)O_4F_2]$ polyhedra the Fe-O bond lengths (1.938(8)-2.011(7) Å for **1** and 1.935(6)-2.000(6) Å for **2**) as well as the Fe-F distances (1.929(7)-1.983(7) Å for **1** and 1.929(6)-1.993(4) Å for **2**) are in good agreement with 3+ oxidation state for the Fe(1) and Fe(2) atoms, based on the bond valence sums (BVS) calculations.[46] Both polyhedra display eight O-Fe-F and four O-Fe-O *cis* angles, and two O-Fe-O and one F-Fe-F *trans* angles. However, in the $[M(3)O_4F_2]$ and $[M(4)O_2(H_2O)_2F_2]$ octahedra, M-O bond lengths span from 2.060(6) to 2.274(8) Å for **1** and from 2.056(4) to 2.216(6) Å for **2**, and the M-F distances are in the ranges 1.996(6)-2.148(7) Å for **1** and 1.994(5)-2.125(5) Å for **2**. In this case, the M-O/F distances indicate at first glance that, from the structural point of view, M(3) and M(4) sites are in +2 state. In these polyhedra the fluorine atoms are located in the edges, giving rise to six O-M-F, five O-M-O and one F-M-F *cis* angles and four O-M-O *cis* angles, and two O-M-F and one O-M-O *trans* angles.

The $S(O_h)$ values for phases **1** and **2**, calculated by Continuous Symmetry Measure,[47] show more distorted octahedra for bivalent metals (M(3) and M(4)), however, they represent very slight distortions with regard to the ideal octahedron.

The P-O distances of the $(HPO_3)^{2-}$ units are in the range 1.482(9)-1.544(8) Å for **1** and 1.493(7)-1.540(6) Å for **2**, and the P-H distances are 1.31(5) Å and 1.32(5) Å for **1** and **2** respectively. The average O-P-O and H-P-O angles are around 112º and 107º respectively for both compounds, which are in the usual range for phosphite based compounds.[48] The terminal P(1)-O(1´) bond distances are significantly higher than the rest of the P-O bonds (1.55(4) for **1** and 1.59(3) for **2**) which could be in good agreement with the existence of $(HPO_4)^{2-}$ groups inferred from the electroneutrality of the formula.

The phosphorus atoms make ten P–O–M (M = Fe, Co) linkages with minimum and maximum values for the P(2)-O(13)-Fe(3) and P(4)-O(8)-Fe(2) angles [123.3(4)º and 160.0(7)º for **1** and 123.5(3)º and 159.1(5)º for **2**].

The octahedra sharing vertex display four M-F-M linkages with average angles of 127.5(3)º for **1** and 128.3(2)º for **2**. The M(3) and M(4) metals share an edge possessing two M-O-M linkages of around 98º and 100º for both phases.

Hydrogen bonding plays an important role linking the tetramine cations to the framework (Fig 3b). The terminal hydrogen-bond donor group, N(1), interact with the oxygens O(6) and O(17W) and the fluorine atoms F(2), and F(4) while the 'internal' donor group, N(2), interact with O(1), O(7), F(1) and F(3). Three C-H···O and one C-H···F contacts are also present in the structures. The complete list of hydrogen bond interactions is shown in Table S6.

In the Cambridge Structural Database (CSD) there are only three structures, based on ionic salts, containing uncomplexed N,N'-Bis(2-aminoethyl)-1,3-propanediamine. In two of them the molecule is a tetracation[49] and in the other one is a trication,[50] with gttttttg (g indicates gauche and t trans) and gttggggt conformations respectively. In the studied compounds, the existence of the symmetry centre forces the splitting of the central carbon (C4) in two positions producing the conformers A and B with conformations not previously seen in the mentioned structures. Given the existence of torsion angles less than 30º and higher than 90º (See torsion angles in Tables S1 and S2), the more systematic Klyne-Prelog system[51] is required to describe them obtaining a ttgaagtt conformation (a = anticlinal) for the conformers A and a ttsaastt conformation (s = synperiplanar) for the conformers B in both compounds.

The amount of potential-free volume was estimated by the program PLATON[52] assuming that the templates could be removed from the channels, being around 20% of the total volume for phases **1** and **2**. The analysis of the volume occupied by these guest molecules was performed using the TOPOS 4.0 program[43] by means of Voronoi–Dirichlet polyhedra (VDP)[53] (Fig. 3a) obtaining a 23% of the crystal volumes. The matching percentage indicates the non-existence of accessible volume.

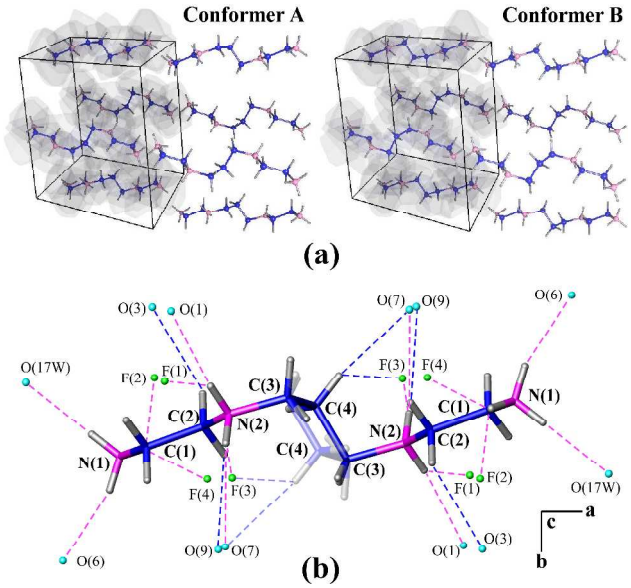

Fig. 3 a) *VDP* representation of the templates located in the voids of the phase **1**. b) Interlayer hydrogen bonds scheme of phase **1**.

Thermal study

The TGA curves of **1**, **2** and **3** show three main weight losses. The results are given in Supporting Information (Fig. S7). The first one (**1**, 80-285 ºC; **2** and **3**, 80-275ºC) is associated to the release of two coordinated water molecules (~4.8 %). Afterwards, there are two drops (**1**, 285-520 ºC; **2** and **3**, 275ºC-540ºC) related to the calcination of the organic molecule (~11.0 %). This second process is marked by three and two exothermic peaks in the DTA (**1**, 285, 315 and 460 ºC) and DSC (**2**, 269 and 287 ºC; **3**, 272 and 292ºC) curves, respectively, due to the breakage of C-C and C-N

bonds. The third process, which is overlapped with the organic molecule decomposition, is assigned to the elimination of the fluoride anions. Two exothermic peaks observed in the DTA (**1**, 535 and 585ºC) and DSC curves (**2** and **3**, 545 and 565 ºC) indicate the crystallization of the inorganic residues.

The thermodiffractometry in air of **1** and **3** reveal that their thermal stability limits are situated at 240 and 255ºC, respectively, in such experimental conditions (Fig. S8). At these temperatures and as a consequence of the elimination of the two coordinated water molecules, the compounds become amorphous and, at 570 ºC the inorganic residues crystallize, in good agreement with the exothermic peaks observed in the DTA and DSC curves. The X-ray powder diffraction patterns of the residues obtained at 800 ºC show the presence of $FePO_4$ [*PDF file:* 00-050-1635; S.G. $P3_121$ (152), a= 5.048 Å, c= 11.215 Å] for **1** and $FePO_4$ [*PDF file: 01-084-0876*; S.G. $P3_121$ (152), a= 5.027 Å, c= 11.234 Å] and $Co_3Fe_4(PO_4)_6$ [*PDF file*: 00-049-1083; S.G. P-1 (2), a= 7.909 Å, b= 9.289 Å, c= 6.342 Å, α= 108.48º, β= 101.52º, γ= 104.67º) for **3**. It is probably that the increase in weight observed during the TGA studies around 450 ºC is due to the oxidation of P(III) to P(V), provoking the crystallization of the mentioned inorganic phosphates. The thermal evolution of the cell parameters for **1** and **3** was determined by pattern matching analysis (Fig. S9). The volume of the phases exhibits a constant increase with thermal expansion coefficients around $40 \cdot 10^{-6}$ and $34 \cdot 10^{-6}$ ºC^{-1} in the 30-195 ºC temperature range.

Infrared, UV-Vis, XPS and Mössbauer spectroscopy

In the infrared spectra of the three compounds (Fig. S10), the organic template is mainly represented by a group of overlapped maxima corresponding to stretching vibrations (ν) of N-H and C-H bonds in the 3100-2500 cm^{-1} region. The $\delta(NH_3^+)$ band appears at 1600 cm^{-1}, indicating that the organic molecules are protonated and not coordinated to the inorganic building.

Regarding the inorganic part, around 2400 cm^{-1} a narrow band split in two ones, corresponding to the stretching vibrational mode of the P-H bond from the $(HPO_3)^{2-}$ groups can be observed in the spectra. At lower frequencies, in the 1100 - 400 cm^{-1} range, the bands corresponding to the P-O bonds vibrations of the phosphite/phosphate groups are observed. The ν(O-H) absorption band related to the coordinated water molecules is also observed at around 3420 cm^{-1}.

The diffuse reflectance spectra of **1**, **2** and **3** show mainly four bands (Fig. 4). In the diffuse reflectance spectrum of **1**, two bands at approximately 10640 and 7520 cm^{-1} are observed. These bands are characteristic of the iron(II) d^6-high spin cation in a slightly distorted octahedral environment, and correspond to the electronic transitions from the $^5T_{2g}(^5D)$ fundamental state to the excited level $^5E_{2g}(^5D)$ that is splitted as a consequence of the existence of the non-regular $[M(3)O_4F_2]$ and $[M(4)O_2(H_2O)_2F_2]$ octahedra. The energy associated with this transition corresponds, according to the Tanabe-Sugano diagram[54] to the *Dq* parameter. The value obtained is *Dq*= 910 cm^{-1}. An overlapped band situated around 13510 cm^{-1} which corresponds to the forbidden transition from the $^6A_{1g}(^6S)$ ground state to the $^4T_{1g}(^4G)$ term is attributed to the presence of iron(III) d^5-high spin configuration cations.[55] An intense band can also be observed at approximately 18180 cm^{-1}. This band is likely to correspond to the intervalence transition between the Fe^{2+} and Fe^{3+} cations, because their polyhedra share the four crystallographically independent fluorine atoms and the intermetallic bond distance are short enough (between 3.57 and 3.69 Å).[27] In the spectra of **2** and **3** compounds the discrimination of the transition bands characteristic of the Co^{2+} cations is not a clear task because of the overlapping of different d^5, d^6 and d^7 high spin cations signals. However, these spectra show a significant change in the relative intensity of the splitted $^5T_{2g}(^5D) \rightarrow {}^5E_{2g}(^5D)$ transition bands as well as a reduction in the intensity of the $t_{2g}(Fe^{2+}) \rightarrow t_{2g}(Fe^{3+})$ intervalence transition, suggesting an effective substitution of Fe(II) by Co(II).

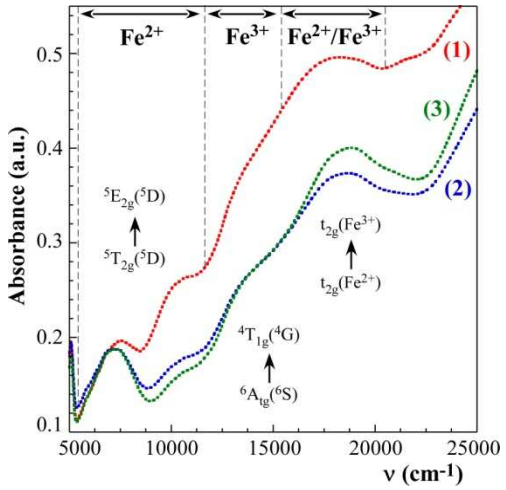

Fig. 4. UV-Vis spectra of iron (II)-(III) **1** (in red) and cobalt(II)-substituted **2** (in blue) and **3** (in green) complexes.

The chemical composition and the possible oxidation state of the iron and cobalt metals of the upper layers in these compounds were investigated by XPS measurements. The fitting together with the binding energies of the N 1s, P 2p, F 1s, Fe 2p and Co $2p_{1/2}$ peaks are deposited as Supplementary material (Fig. S11).

The N 1s peaks are resolved into two peaks at around 399 and 401 eV which could be attributed to the existence of two primary and two secondary protonated amines per organic molecule. The P 2p peaks are deconvoluted into two doublets registered at binding energies between 130 and 133 eV and assigned to P(III) species, which used to be lower than observed for P(V) species.[56] The F 1s peak centered at around 684 eV may be attributed to the metal-fluorine bonds.[57] The decomposition of Fe $2p_{3/2}$ spectra for compound **1** suggests the coexistence of Fe^{2+} close to 711 eV and Fe^{3+} at around 714 eV according to the values found for FeF_2·and FeF_3 fluorides, respectively.[58] Deconvolution of this region in compounds **2** and **3** is hindered by the interference of the Auger line Co LMM, however, the values of the Fe $2p_{1/2}$ component close to 724 and 727 eV, next to those found in **1**, suggests also the mixed valency of the iron cations. Moreover, it is important to note the absence of the satellite peak of the Fe 2p as it has been previously reported for the mixed valence iron oxide Fe_3O_4.[59] Likewise, compounds **2** and **3** show a Co $2p_{1/2}$ main line at a binding energy around 797 eV, which is close to that found in a recently published cobalt(II) hybrid phosphite.[60] The presence of the strong satellite peak at about 6 eV from the Co $2p_{1/2}$ component is a further evidence for Co^{2+} species.[61]

The powder ^{57}Fe room temperature Mössbauer spectra of the three compounds were studied as shown in Fig. 5. The best fit of

1, **2** and **3** leads to one doublet for iron(III) cations and another one for iron(II), obtaining Fe^{3+}/Fe^{2+} area ratios of 1.35, 2.80 and 3.20 respectively. The values of the isomer shift and quadrupolar splitting parameters given in Table 2 show the characteristic values for the Fe^{3+} and Fe^{2+} cations. Given the multiplicity of the four crystallographically independent positions for the iron atoms and the metal-ligand distances obtained from the single-crystal structure analysis of compound **1**, the Fe^{3+} are distributed over the positions Fe(1) and Fe(2) and the Fe^{2+} in the M(3) and M(4) positions. However, the percentage of Fe^{3+} exceeds 50%, so we interpret that a partial substitution of Fe(II) by Fe(III) (Occ. = 0.296) occurs in the M(3) position (Fig. 6) as this presents a less variation of the metal-ligand distances range than the $M(4)O_2(H_2O)_2F_2$ octahedron.

Taking into account the structural features of compound **2**, it is assumed that the Fe^{3+} ions occupy only the Fe(1) and Fe(2) positions. Therefore, considering the amount of cobalt obtained from the ICP-Q-MS analysis and the results from the structural refinement, the Fe^{2+} are totally replaced by Co^{2+} ions in the M(4) position and partially substituted in the M(3) position (Occ. = 0.290) (Fig. 6).

Table 2 Hyperfine parameters at 298 K (δ, isomer shift; ΔE, quadrupolar splitting; %, proportion of each component) for **1**, **2** and **3**

	Position	*δ (mm/s)*	*ΔE (mm/s)*	*(%)*
1	$(Fe(1)+Fe(2))^{3+}$	0.313(1)	0.42(1)	57.4
	$(M(3)*+M(4))^{2+}$	1.150(1)	2.61(1)	42.6
	* 7.4% that exceeds the 50% of Fe^{3+} occupies M(3) position			
2	$(Fe(1)+Fe(2))^{3+}$	0.318(1)	0.44(1)	73.7
	$M(3)^{2+}$	1.165(1)	2.62(1)	26.3
3	$(Fe(1)+Fe(2))^{3+}$	0.314(1)	0.44(1)	76.2
	$M(3)^{2+}$	1.187(1)	2.57(1)	23.8

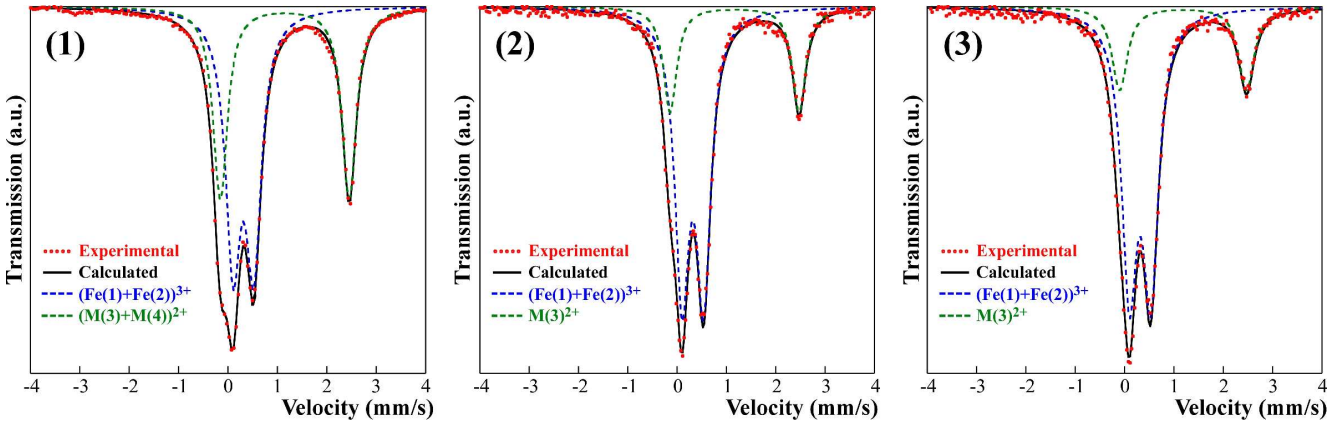

Fig. 5 Mössbauer spectra of **1**, **2** and **3** at room temperature.

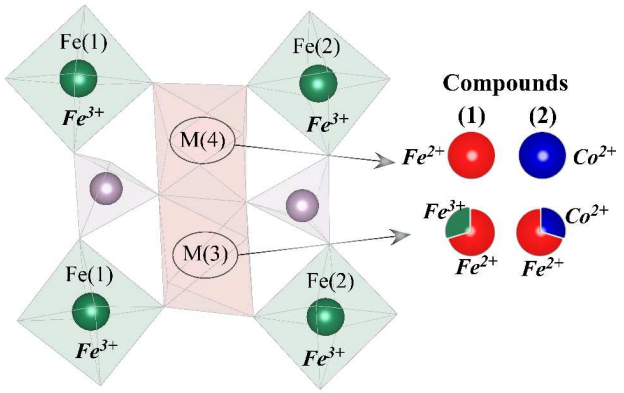

Fig. 6. Distribution of the Fe^{3+}, Fe^{2+} and Co^{2+} cations inferred from the structural analysis and the Mössbauer study.

Magnetic behaviour of 1 and 3

Fig. 7 shows the temperature dependence of the molar magnetic susceptibility (χ_m) and inverse susceptibility ($1/\chi_m$) curves of compounds **1** and **3**, measured on powdered samples from room temperature to 2 K, in the Field Cooling (FC) mode at 2 kOe.

The molar magnetic susceptibility of **1** and **3** continuously increases as temperature decreases, showing a typical paramagnetic behaviour above 40 K. At lower temperatures, χ_m curve of **1** reaches a width rounded maximum at approximately 28 K, showing a minimum at 20 K and then increasing again with an inflection point close to 6 K. A similar behaviour was observed in the compound $Co_2(OH)AsO_4$.[62] However, the behaviour of **3** at low temperatures is somewhat different, in such a way that the maximum which FC curve displays at 28 K is quite sharp, besides that the susceptibility decreases much more than **1** after the maximum, reaching a minimum at approximately 10 K. Afterwards, χ_m curve increases until 2K without changes in curvature. These behaviours at low temperature do not correspond either to a typical ferromagnet or antiferromagnet, although it looks more like that observed in antiferromagnets, specially in **3**.

The experimental data in both cases follow the Curie-Weiss law above 100 K (see lower insets in Fig. 7), allowing the calculation of the Weiss temperature (**1**, θ = -95.6 K and **3**, θ = -125 K) and the average effective paramagnetic moment per metal ion (**1**, μ_{eff}= 5.60 μB and **3**, μ_{eff}= 5.95 μB). The value of μ_{eff} for **1** is intermediate between the expected for Fe^{2+} (5.4 μ_B) and Fe^{3+} (5.9 μ_B), whereas that for cobalt-substituted compound is slightly higher than the expected for Fe^{3+}, probably because the Co ions present an extra contribution coming from the angular momentum. The negative Weiss temperatures together with the

decrease of the $\chi_m T$ products with decreasing temperature indicate that the main magnetic interactions in these compounds are antiferromagnetic. The abrupt increase of the susceptibility below 20 K for **1** and the sharp maximum close to 28 K for **3** correspond to the onset of AF order, as will be described later from M(H) curves and heat capacity (Cp) data.

The upper insets of Fig. 7 show the low temperature ZFC and FC molar susceptibility (χ_m) details performed at 0.5, 2 and 10 kOe. For **1** a small irreversibility appears at 0.5 kOe below 30K and although practically disappears for fields higher than 2 kOe, a tiny contribution persists up to 10 kOe. For **3** a small splitting of the curves can also be observed but whose intensity is much less dependent on the magnetic field than in the compound **1**. Besides, the minimum location is reliant on the magnetic field, shifting from 9 to 16 K as increasing the field from 0.5 to 10 kOe for **3**, while for **1** the position remains practically unchanged at 20K regardless of the applied field. The existence of irreversibility can only be attributed to the existence of a weak ferromagnetic component.

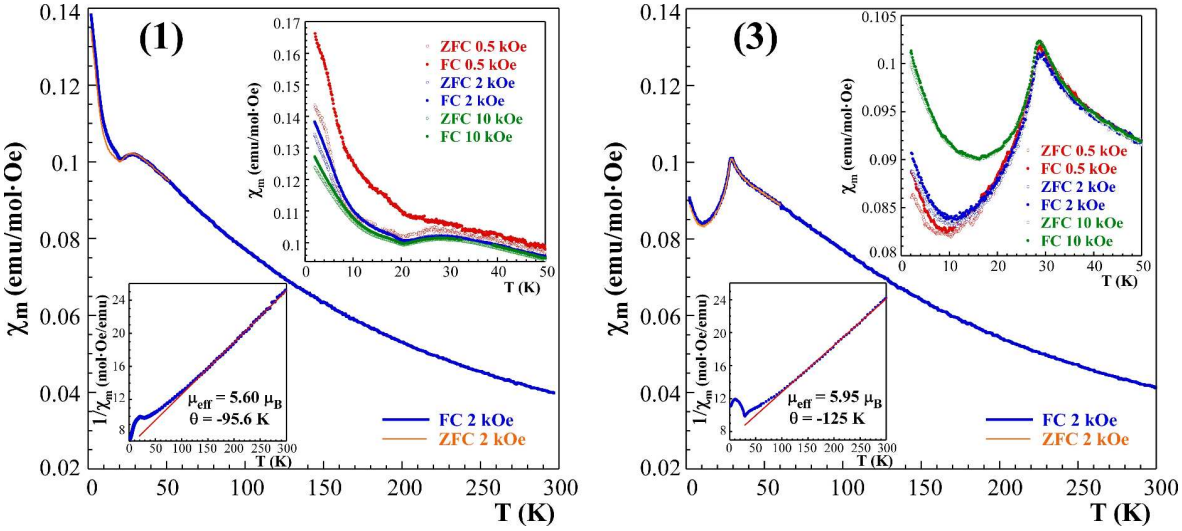

Fig. 7 Temperature dependence of χ_m for compounds **1** and **3** measured under 2 kOe. The lower inset shows the $1/\chi_m$ curve fitted to the Curie−Weiss law and the upper inset an enlargement of the low-temperature region of ZFC−FC data measured under 0.5, 2 and 10 kOe.

In Fig. 8a it is depicted the field dependence of the magnetization of **1** at different temperatures. At 2 K, the magnetization increases almost linearly with the magnetic field until a critical field of 45 kOe, where a metamagnetic transition occurs. The magnetization value ($0.45\mu_B$/Fe ion) obtained at the highest applied field, 90 kOe, is far from the theoretical saturation for the Fe(II) ($4\mu_B$) and Fe(III) ($5\mu_B$) ions, indicating the existence of a strong magnetocrystalline anisotropy. Despite the M(H) general behaviour is characteristic of an antiferromagnetic order, it is important to note the existence of an small hysteresis with a coercitive field of 85 Oe at low temperatures, which confirms the existence of a weak ferromagnetic component (lower inset in Fig 8a).

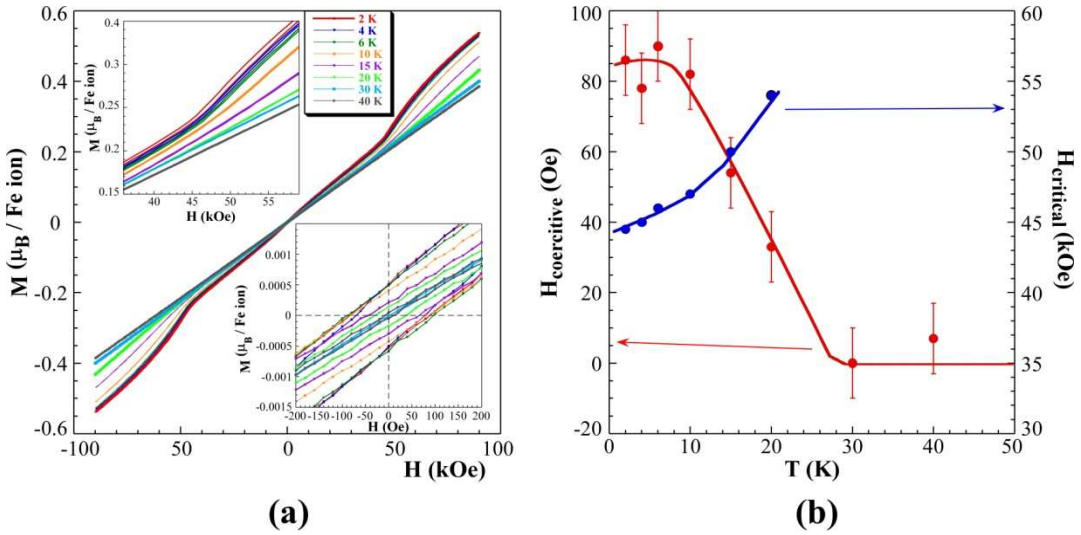

Fig. 8 a) Magnetization vs applied magnetic field at different temperatures for **1**. The upper inset shows the detail of the metamagnetic transition and the lower inset an enlargement of the small coercitivity of the hysteresis loops. b) Thermal evolution of the coercitive field of the hysteresis loops and critical field of the metamagnetic transition.

Cite this: DOI: 10.1039/c0xx00000x

www.rsc.org/xxxxxx

ARTICLE TYPE

The hysteresis decreases as the temperature increases, disappearing in the paramagnetic region. The temperature increase also provokes a positive shift of the critical field of the metamagnetic transition (upper inset in Fig 8a). Above 20K, the metamagnetic transition disappears as well as the M(H) curves are completely linear up to 90 kOe (Fig. 8b). In the case of compound **3**, the hysteresis loops do not show any significant remnant magnetization. However, there is also a critical field close to 62 kOe at 2K indicating the existence of a metamagnetic transition (Fig. S12, Supplementary Material).

To get a further insight of the weak ferromagnetic component of **1**, we have measured the thermoremanent magnetization (TRM) as well as the ac magnetic susceptibility. The TRM curve was measured at H = 0 after cooling from $T \geq T_N$ under a magnetic field of 5 kOe. As can be observed in Fig. S13, the value decreases continuously as increase the temperature, reaching zero above the Neel temperature. The appearance of a positive remanent magnetization below T_N confirms the existence of a weak ferromagnetic component. In addition, it is important to signal the appearance of a clear shoulder at around 6 K as was also pointed out in the FC curve. The real (χ') and imaginary (χ'') components of the ac susceptibility at 1000 Hz with an ac field of 10 Oe are shown in Fig. S14. χ'shows a broad maximum centred at 28 K (T_N) whereas χ'', which should be zero in antiferromagnetic compounds, has a small contribution associated with the weak ferromagnetic component. Surprisingly a sharp peak emerges in both $\chi'$and χ'' around 4.5 K indicating the presence o a magnetic transition of different nature from the previous one. This transition was masked in the magnetic susceptibility by the weak ferromagnetic component but should be the responsible of the shoulder observed around 6 K in the FC and TMR curves. To check the origin of this low temperature transition we have measured the ac susceptibility at different frequencies (inset of Fig. S14). The peak height decreases and the position of the maximum shifts to higher temperatures with increasing frequency, as usually happens in spin glass transitions. The spin glass nature of the transition is further confirmed by the absence of any anomaly at 4.5 K in the heat capacity data. The coexistence of antiferromagnetism and spin glass behaviours has been previously observed in other insulator materials.[23,63] This result could be due to the simultaneous but random presence of Fe(II) and Fe(III) cations in the M(3) position of compound **1** (Fig. 6), which gives rise to the competing interactions. Both randomness and competing interactions lead to spin frustration, ultimately resulting in the spin-glass state.

Considering the structural features of compounds **1** and **2**, studied by single crystal X-ray diffraction, and taking into account that **3** is isotypic, several magnetic pathways can take place in these three phases. Inside the layers metal–metal distances range between 3.2 and 3.7 A° and consequently direct interactions are not negligible. A view of the most important magnetic exchange interactions M–O–M and M-F-M in **1** and **2** is given in Fig. S15. J_1 pathway represents direct intradimeric magnetic interactions via oxygen atoms between the $M(3)O_4F_2$ and $M(4)O_2(H_2O)_2F_2$ polyhedra. The values of the bond angles for J_1 are around 98º and 100º, being able to lead to a ferromagnetic interaction inside the dimers. However, J_2 to J_5 pathways imply superexchange interactions through fluorine atoms involving bond angles between approximately 124 and 133º and clearly indicating the existence of an antiferromagnetic coupling. The superexchange inter- and intralayer M–O–P–O–M interactions allows one to propagate the magnetic interactions giving rise to a three-dimensional magnetic system. The bond distances and angle values for the exchange pathways are very close for **1** and the cobalt substituted compounds **2** and **3**. So, the differences in the magnetic properties from **1** to **3** cannot be explained from a structural point of view.

Taking into account that the Co^{2+} ions prefer the $M(3)O_4F_2$ and $M(4)O_2(H_2O)_2F_2$ octahedra, the substitution of Fe(II) (d^6) (S = 2) by Co(d^7) (S = 3/2) in the framework of **1** modifies the nature of some magnetic interactions involving J_1 pathway.

The specific heat curves represented in Fig. 9 show a small maximum centered at 20.5 K for **1** and a sharp magnetic peak at 28 K for **3**. Despite the anomaly observed for **1** does not have the typical appeareance of a λ-type second-order transition peak as in the case of the cobalt containing compound, it can be associated with the establishment of a three-dimensional antiferromagnetic order in good arrangement with the magnetic-susceptibility data. It is important to signal the absence of any additional anomaly at low temperatures, confirming the spin glass nature of the transition observed in the ac susceptibility at 4.5 K. The continuous growth of Cp at higher temperatures is due to the lattice contribution (Cp_{pho}), which does not show any tendency to saturation. In fact, the Cp values at 300 K for both compounds are around 660 J/molK, still far from the expected values (**1**, 1287.8 and **3**, 1294.0 J/molK) according to the Dulong and Petit law for the 51.6 and 51.9 ions per unit formula for **1** and **3**, respectively. This is due to the presence of light atoms with very high excitation energy.

In order to extract the magnetic contribution, C_{mag}, the Cp_{pho} was estimated using the Debye model and considering the existence of three Debye temperatures (the minimum number of free parameters that will allow us to fit the experimental data). In this way, if the number of atoms in the unit cell is N, we suppose n_1 atoms with a Debye temperature θ_{D1}, n_2 atoms with a Debye temperature θ_{D2}, and $n_3 = (N-n_1-n_2)$ atoms with a Debye temperature θ_{D3}. Therefore, there are five free parameters, namely, n_1, n_2, θ_{D1}, θ_{D2}, and θ_{D3}. This approach has been used successfully in previous studies in other hybrid compounds.[64] The best fittings are obtained for n_1 = 10.2, θ_{D1}= 213 K, n_2 = 15.6, θ_{D2}= 650 K and θ_{D3}= 2350 K for compound **1** (N = 51.6) and n_1 = 10.9, θ_{D1}= 232 K, n_2 = 15.6, θ_{D2}= 689 K and θ_{D3}= 2578 K for compound **3** (N = 51.9). The good quality of the fits (see the continuous lines in Fig. S.16) allows us to consider that this phenomenological model determines reasonably well the phonon contribution. The magnetic contribution, obtained as Cp_{mag} = Cp

− Cp_{pho}, is plotted in the insets of Fig. S16 (a) and (b) for compounds **1** and **3** respectively. The value of Cp_{mag} in the maximum is clearly larger for **3,** 46.5 J/mol K, than for **1**, 34.5 J/mol K. In addition, whereas for **3** Cp_{mag} has a λ-peak shape, for **1**, Cp_{mag} has a triangular shape, extending up to 60 K. These findings also indicates that compound **1** has a more complex magnetic structure than compound **3**.

Heat-capacity has been also studied in the presence of several magnetic fields. With increasing field for **3**, the sharp λ-type magnetic peak becomes more rounded and shifts to lower temperatures, what is in good agreement with a global antiferromagnetic behaviour as was also observed from the magnetic susceptibility. In the case of compound **1**, an unexpected behaviour was observed. The small maximum shifts to higher temperatures, grows with the magnetic field and becomes better defined. Usually, the effect of the magnetic field on ferromagnetic transitions consists of shifting the λ anomaly to higher temperatures making it more rounded and less height.

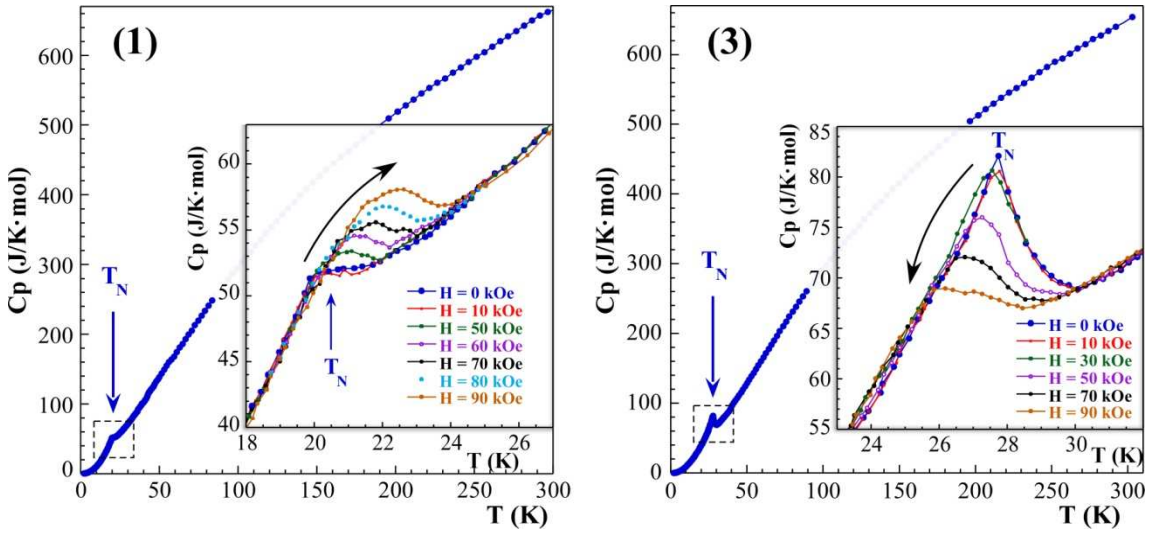

Fig. 9 Specific heat of compounds **1** and **3** between 2 and 300 K. The insets show an enlargement around the Neel temperature as a function of temperature in the presence of external magnetic fields, H, in the 0-90 kOe range.

Therefore, the small value of the anomaly observed in **1** could be associated with an incommensurate magnetic structure, in which the entropy difference with the paramagnetic state is lower than in commensurate structures. The proposal of this kind of structure is also supported by the behaviour of the anomaly with the applied magnetic field. A similar behaviour of the specific heat anomaly was observed in the compound $Co_2(OH)AsO_4$,[62] and in that case it was interpreted as an evolution of the magnetic structure to the commensurability.

Conclusions

The mild hydrothermal technique was used for the synthesis of three novel 3D open-framework fluorinated mixed valence Fe(II)-Fe(III) phosphites with channels templated by protonated tetramine chains. The combined information from chemical analysis, X-ray diffraction and Mössbauer spectroscopy has allowed us to determine the Fe^{3+}, Fe^{2+} and Co^{2+} cation distribution over the four metal sites. While Fe(1) and Fe(2) positions have a full occupancy of Fe^{3+} in the three phases, M(4) is occupied by Fe^{2+} in **1** but totally replaced by Co^{2+} in **2** and **3**. M(3) position presents partial occupations: 0.30 Fe^{3+}:0.70 Fe^{2+} for **1**, 0.29 Co^{2+}:0.71 Fe^{2+} for **2** and 0.38 Co^{2+}:0.62 Fe^{2+} for **3**.

The average structure resolution of **1** neglecting the satellite intensity leaves electron density peaks above $\pm 3e^{-}\cdot Å^{-3}$, which are found at the equatorial plane of the $[M(4)O_2F_2(H_2O)_2]$ octahedron and near the nitrogen N(2) atom belonging to the organic template. The reciprocal analysis of **1** shows satellite reflections, described by a q = 0.284(2)a*, which are the result of an incommensurate long-range order involving the crystallographic [100] direction. It is logical to think that the incommensurate structure is related to an incommensurate disorder of the organic molecule located along the [100] channels within the inorganic framework. This long-range order of the template seems to affect also the inorganic skeleton, because of the extensive network of hydrogen bonds, as it is deduced from the residual electron densities located near the M(4) and P(4) sites. This incommensurability is not observed in **2**. Therefore, while the template movement along the *a* axis describes a structural modulation of the structure of **1**, in **2** has not a periodic character, only observing local disorders.

Magnetic measurements of **1** and **3** are consistent with the existence of major antiferromagnetic interactions. Compound **1** also exhibits weak ferromagnetism at low temperature and an additional spin glass transition at the freezing temperature T_f = 4.5 K. Despite the expected increase in random magnetic interactions with Co substitution because of its anisotropic nature, the freezing temperature and the weak ferromagnetism disappears in compound **3**. So, the presence of Co(II) ions in both M(3) and M(4) sites and in particular the suppression of the random mixed valency of the iron cations in M(3) site can reduce drastically the magnetic frustration.

Specific heat curves show a small anomaly at 20.5 K for **1** and a sharp magnetic peak at 28 K for **3**. Strikingly, the anomaly observed in **1** grows with the magnetic field and becomes better defined. Such characteristics as the low value and its behaviour with the applied magnetic field suggest that this is due to the existence of an incommensurate magnetic structure as was interpreted in compound $Co_2(OH)AsO_4$. In fact, the existence of

residual electron density peaks located in the M(4) site, occupied by Fe(II) cations, inevitably seems to have some kind of relationship with the incommensurate magnetic structure of **1**. In addition, the specific heat study of the cobalt-substituted phase **3** does not show signs of the existence of an incommensurate magnetic structure at low temperatures. It should be recalled that M(4) site is totally occupied by Co(II) ions in phases **2** and **3** and does not show significant residual maxima around as was observed in the structural study of **2**.

Acknowledgments

This work has been financially supported by the "Ministerio de Ciencia e Innovación" (MAT2010-15375 and MAT2011-27573-C04), the "Gobierno Vasco" (IT630-13) and the "UPV/EHU" (UFI11/15), which we gratefully acknowledge. The authors thank the technicians of SGIker (UPV/EHU), financed by the National Program for the Promotion of Human Resources within the National Plan of Scientific Research, Development and Innovation, "Ministerio de Ciencia y Educación" and "Fondo Social Europeo" (FSE), for the X-ray diffraction, XPS, chemical and spectroscopic measurements. J. Orive wishes to thank the Universidad del País Vasco, UPV/EHU for funding.

Notes and references

[a] *Departamento de Mineralogía y Petrología, Facultad de Ciencia y Tecnología, Universidad del País Vasco (UPV/EHU), Apdo. 644, 48080 Bilbao, Spain. Fax:+34 946 013 500; Tel: +34 946 015 984; E-mail: joseba.orive@ehu.es, roberto.fernandez@ehu.es, maribel.arriortua@ehu.es.*

[b] *CITIMAC, Facultad de Ciencias, Universidad de Cantabria, 39005 Santander, Spain. Fax:+34 942 201 402; Tel: +34 942 201 511; E-mail: rodrigufj@unican.es.*

[c] *Departamento de Electricidad y Electrónica, Facultad de Ciencia y Tecnología, Universidad del País Vasco (UPV/EHU), Apdo. 644, 48080 Bilbao, Spain. Fax:+34 946 013 500; Tel: +34 946 015 940; E-mail: estibaliz.legarra@ehu.es, fernando.plazaola@ehu.es.*

† Electronic Supplementary Information (ESI) available: View of the reciprocal space and reconstruction of the h0l layers of **1** and **2**, **c**onformers A and B of the organic molecule, Rietveld structure analysis of **3**, thermal ellipsoid plots of **1** and **2**, thermal analysis, infrared spectra, XPS spectra, magnetization *vs* applied magnetic field at different temperatures for **3**, thermoremanent magnetization and ac magnetic susceptibility for **1**, magnetic pathways and thermal evolution of Cp, Cphon, and Cmag of phases **1** and **3**. CCDC 978254 and 978255. See DOI: 10.1039/b000000x/

1 D. Maspoch, D. Ruíz-Molina, J. Veciana, *Chem. Soc. Rev.*, 2007, **36**, 770.

2 S. Natarajan, S. Mandal, *Angew. Chem. Int. Ed.*, 2008, **47**, 4798.

3 M. E. Davis, *Nature*, 2002, **417**, 813; E. R. Parnham and R. E. Morris, *Acc. Chem. Res.*, 2007, **40**, 1005; J. Jiang, J. Yu and A. Corma, *Angew.Chem., Int. Ed.*, 2010, **49**, 3120.

4 J. Yu, R. Xu, *Accounts Chem. Res.*, 2010, **43(9)**, 1195.

5 T. Loiseau, G. Férey, *J. Mater. Chem.*, 1996, **6**, 1073; C. Sassoye, J. Marrot, T. Loiseau, G. Ferey, *Chem. Mater.*, 2002, **14**, 1340.

6 J. Orive, E. S. Larrea, R. Fernández de Luis, M. Iglesias, J. L. Mesa, T. Rojo, M. I. Arriortua, *Dalton Trans.*, 2013, **42**, 4500; H-L. Huang, S-L. Wang, *Chem. Commun.*, 2010, **46**, 6141.

7 Y. Yang, N. Li, H. Song, H. Wang, W. Chen, S. Xiang, *Chem. Mater.,* 2007, **19**, 1889. J. Li, L. Li, J. Liang, P. Chen, J. Yu, Y. Xu, R. Xu, *Cryst. Growth Des.*, 2008, **8(7)**, 2318; J. Liang; J. Li, J. Yu, P. Chen, Q. Fang, F. Sun, R. Xu, *Angew. Chem. Int. Ed.,* 2006, **45**, 2546.

8 R. Chao, Y. Kong, L. Jin, Y. Ren, Y. Ding, N. Li, N. Guan, S. Xiang, *Microporous Mesoporous Mater.*, 2013, **176**, 132.

9 H-Y. Lin, C-Y. Chin, H-L. Huang, W-Y. Huang, M-J. Sie, L-H. Huang, Y-H. Lee, C-H. Lin, K-H. Lii, X. Bu, S-L. Wang, *Science*, 2013, **339**, 811.

10 P. Feng, X. Bu, G. D. Stucky, *Nature*, 1997, **388**, 735; X. Bu, P. Feng, G. D. Stucky, *J. Am. Chem. Soc.*, 1998, **120**, 11204.

11 A. Choudhury, S. Natarajan, C. N. R. Rao, *Inorg. Chem.*, 2000, **39**, 4295.

12 S. Natarajan, *Chem. Commun.*, 2002, 780.

13 J. A. Rodgers, W. T. A. Harrison, *J. Mater. Chem.*, 2000, **10**, 2853.

14 W-M. Chang, M-Y. Cheng, Y-C. Liao, M-C. Chang, S-L. Wang, *Chem. Mater.*, 2007, **19**, 6114.

15 M. E. Davis, R. F. Lobo, *Chem. Mater.*, 1992, **4**, 756.

16 D. W. Lewis, D. J. Willock, C. R. A. Catlow, *Nature*, 1996, **382**, 604; J. Li, J. Yu, R. Xu, *Microporous Mesoporous Mater.,* 2007, **101**, 406; R. Pophale, F. Daeyaert, M. W. Deem, *J. Mater. Chem. A*, 2013, **1**, 6750.

17 A. Lu, N. Li, Y. Ma, H. Song, D. Li, N. Guan, H. Wang, S. Xiang, *Cryst. Growth Des.*, 2008, **8(7)**, 2377.

18 A. Lakiss, A. Simon-Masseron, F. Porcher, S. Rigolet and J. Patarin, *Eur. J. Inorg. Chem.*, 2007, 25, 4043; X. Luo, D. Luo, M. Gong, Y. Chen, Z. E. Lin, *CrystEngComm.*, 2011, **13**, 3646; L. Xue, D. Luo, X. Luo, H. Zeng, Z. Lin, *Solid State Sciences*, 2013, **19**, 80.

19 G-M. Wang, J-Q. Jiao, X. Zhang, X-M. Zhao, X. Yin, Z-H. Wang, Y-X. Wang, J-H. Lin, *Inorg. Chem. Comm.*, 2014, **39**, 94; L-M. Li, K. Cheng, F. Wang, J. Zhang, *Inorg. Chem.*, 2013, **52(10)**, 5654; G. Wang, J. Li, X. Zhang, P. Wang, B. Pang, Z. Wang, Y. Wang, J. Lin, C. Pan, *Dalton Trans.*, 2013, **42**, 13084.

20 T. Rojo, J. L. Mesa, J. Lago, B. Bazán, J. L. Pizarro, M. I. Arriortua, *J. Mater. Chem.*, 2009, **19**, 3793.

21 W. Yang, J. Li, Q. Pan, H. Xing, Y. Chen, J. Yu, R. Xu, *J. Mater. Chem.*, 2009, **19**, 4523; S. Mandal, S. Natarajan, J. M. Grenèche, M. Riou-Cavellec, G. Férey, *Chem. Mater.*, 2002, **14**, 3751.

22 G. Paul, A. Choudhury, E. V. Sampathkumaran, and C. N. R. Rao, *Angew. Chem. Int. Ed.*, 2002, **41(22)**, 4297.

23 U-C. Chung, J. L. Mesa, J. L. Pizarro, I. de Meatza, M. Bengoechea, J. Rodríguez Fernández, M. I. Arriortua, T. Rojo, *Chem. Mater.,* 2011, **23**, 4317.

24 B. Bazan, J. L. Mesa, J. L. Pizarro, A. Peña, M. I. Arriortua, T. Rojo, *Z. Anorg. Allg. Chem.*, 2005, **631**, 2026.

25 J. Orive, J. L. Mesa, E. Legarra, F. Plazaola, M. I. Arriortua, T. Rojo, *J. Solid State Chem.*, 2009, **182**, 2191.

26 Y. Fan, T. Song, G. Li, Z. Shi, G. Yu, J. Xu, S. Feng, *Inorg. Chem. Commun.*, 2005, **8(8)**, 661.

27 S. Fernández-Armas, J. L. Mesa, J. L. Pizarro, M. I. Arriortua, T. Rojo, *Mater. Res. Bull.*, 2007, **42(3)**, 544.

28 S. Fernández-Armas, J. L. Mesa, J. L. Pizarro; J. S. Garitaonandia, Arriortua, M. I. Arriortua, T. Rojo, *Angew. Chem. Int. Edit.*, 2004, **43(8)**, 977.

29 F. Shiba, R. Fujishiro, T. Kojima, Y. Okawa, *J. Phys. Chem. C*, 2012, **116**, 3394;

30 Q. Lin, C. Lei, G. Tang,·Q. Zhang, Y. He, *Hyperfine Interact.*, 2013, **219**, 95; E. Coronado, J. R. Galán-Mascarós, C. J. Gómez-García, V. Laukhin, *Nature*, 2000, **408**, 447.

31 O. Sato, T. Iyoda, A. Fujishima, K. Hashimoto, *Science*, 1996, **172**, 704.

32 J. -H. Park, E. Izmár, M. W. Meisel, Y. -D. Huh, F. Frye, S. Lane, D. R. Talham, *Appl. Phys. Lett.*, 2004, **85**, 3797; J. -H. Park, F. Frye, S. Lane, E. Izmár, Y. -D. Huh, D. R. Talham, M. W. Meisel, *Polyhedron*, 2005, **24**, 2355.

33 T. Liu, Y-J. Zhang, S. Kanegawa, O. Sato, *J. Am. Chem. Soc.*, 2010, **132**, 8250; S. Gawali-Salunke, F. Varret, I. Maurin, C. Enachescu, M. Malarova, K. Boukheddaden, E. Codjovi, H. Tokoro, S. Ohkoshi, K. Hashimoto, *J. Phys. Chem. B*, 2005, **109**, 8251; N. Shimamoto, S. Ohkoshi, O. Sato, K. Hashimoto, *Inorg. Chem.*, 2002, **41**, 678; A. Goujon, F. Varret, V. Escax, A. Bleuzen, M. Verdaguer, *Polyhedron*, 2001, **20**, 1339.

34 H-M. Hu, X-Y. Huang, H-S. Sun, D-L. Long, J-S. Huang, X-Z. You, *J. Coord. Chem.*, 1999, **47**, 531; I. P-Y. Shek, W-F. Yeung, T-C. Lau, J. Zhang, S. Gao, L. Szeto, W-T. Wong, *Eur. J. Inorg. Chem.*, 2005, 364; J-e. Koo, D-h. Kim, Y-S. Kim, Y. Do, *Inorg. Chem.*, 2003, **42**, 2983; A. Escuer, R. Vicente, M. S. El Fallah, X. Solans, M. Font-Bardia, *Inorg. Chim. Acta*, 1996, **247**, 85. R. Vicente, A. Escuer, J. Ribas, M. S. El Fallah, X. Solans, M. Font-Bardia, *Inorg. Chem.*, 1993, **32**, 1920.

35 J. Qiao, L. Zhang, Y. Yu, G. Li, T. Jiang, Q. Huo, Y. Liu, *J. Solid State Chem.*, 2009, **182**, 1929.

36 W. Yingua, *J. Appl. Crystallogr.*, 1987, **20**, 258.

37 A. C. T. North, D. C. Philips, F. S. Mathews, *Acta Crystallogr.*, 1968, **A24**, 351.

38 *CrysAlisPro CCD* and *RED*, version 171.35.19; Oxford Diffraction, Ltd.: Oxford, U.K., 2011.

39 G. M. Sheldrick, *SHELXS 97: Program for the Solution of Crystal Structures*, University of Göttingen, Germany, 1977.

40 G. M. Sheldrick, *SHELXL 97: Program for the Refinement of Crystal Structures*, University of Göttingen, Germany, 1977.

41 L. J. Farrugia, *J. Appl. Crystallogr.*, 1999, **32**, 837.

42 E. Dowty, *ATOMS: A Computer Program for Displaying Atomic Structures*, Shape Software, 512 Hidden Valley Road, Kingsport, TN, 1993; K. Momma, F. Izumi, *J. Appl. Crystallogr.*, 2008, **41**, 653.

43 V. A. Blatov, *IUCr CompComm. Newslett.*, 2006, **7**, 4.

44 J. Rodríguez-Carvajal, *Rietveld Pattern Matching Analysis of Powder Patterns*, *FULLPROF*, 1994.

45 R. A. Brand, J. Lauer, D. M. Herlach, *J. Phys F: Met. Phys.*, 1983, **13**, 675.

46 I. D. Brown, D. Altermatt, *Acta Crystallogr.*, 1985, **B41(4)**, 244.

47 S. Álvarez, D. Avnir, M. Llunel, M. Pinsky, *New. J. Chem.*, 2002, **26**, 996; M. Llunel, D. Casanova, J. Cirera, J.M. Bofill, P. Alemany, S. Álvarez, M. Pinski, D. Yatumir, *SHAPE v1.1a: Program for Continuous Shape Measure Calculations of Polyhedral Xn and MLn Fragments*, 2003.

48 J. Loub, *Acta Crystallogr.*, 1991, **B47(4)**, 468.

49 X-C. Su, H-K. Lin, S. R. Zhu, L-H. Weng, X-B. Leng, Y-T. Chen, *Supramol. Chem.*, 2002, **14**, 41; H. B. Szczesniak, V. Patroniak, W. Radecka-Paryzek, M. Kubicki, *Acta Cryst.*, 2009, **C65**, 371.

50 V. Patroniak, W. Radecka-Paryzek, M. Kubicki, *Acta Cryst.*, 2008, **C64**, 511.

51 E. V. Anslyn, D. A. Dougherty, *"Modern Physical Organic Chemistry"*, University Science Books (2006).

52 A. L. Spek, *J. Appl. Crystallogr.*, 2003, **36**, 7; A. L. Spek, *Acta Crystallogr., Sect. D: Biol. Crystallogr.*, 2009, **65**, 148.

53 M. Ókeeffe, *Acta Crystallogr., Sect. A: Cryst. Phys., Diffr., Theor. Gen. Crystallogr.*, 1979, **35**, 772; V. A. Blatov, A. P. Shevchenko, V. N. Serezhkin, *Acta Crystallogr., Sect. A: Found. Crystallogr.*, 1995, **51**, 909; V. A. Blatov, A. P. Shevchenko, *Acta Crystallogr.*, *Sect. A: Found. Crystallogr.*, 2003, **59**, 34.

54 Y. Tanabe, S. Sugano, *J. Phys. Soc. Jpn.,* 1954, **9**, 753.

55 U-C. Chung, J. L. Mesa, J. L. Pizarro, J. Rodríguez Fernández, J. Sánchez Marcos, J. S. Garitaonandia, M. I. Arriortua, T. Rojo, *Inorg. Chem.*, 2006, **45(22)**, 8965.

56 V. V. Guliants, J. B. Benziger, S. Sundaresan, *J. Catal.*, 1995, **156**, 298.

57 X-Z. Liao, Y-S He, Z-F. Ma, X-M. Zhang, L. Wang, *J. Power Sources*, 2007, **174**, 720.

58 J. F. Moulder, W. F. Stickle, P. E. Sobol, K. D. Bomben, "*Handbook of X-ray Photoelectron Spectroscopy (XPS)*", Edited by J. Chastain, Published by Physical Electronics Division, Perkin-Elmer Corporation (1992-1995).

59 T. Yamashita, P. Hayes, *Appl. Surf. Sci.*, 2008, **254**, 2441.

60 X. Wang, Y. Yan, J. Wu, Z. Dong, L. Li, J Li, *Z. Anorg. Allg. Chem.*, 2013, **639(12-13)**, 2343.

61 L. F. Liotta, G. Di Carlo, G. Pantaleo, A. M. Venezia, G. Deganello, *Appl. Catal. B-Environ.*, 2006, **66**, 217.

62 I. de Pedro, J. M. Rojo, J. Rodríguez Fernández, M. T. Fernández-Díaz, T. Rojo, *Phys. Rev. B*, 2010, **81**, 134431.

63 I. de Pedro, J. M. Rojo, J. M. Pizarro, J. Rodríguez Fernández, J. Sánchez-Marcos, M. T. Fernández-Díaz, M. I. Arriortua, T. Rojo, *J. Mater. Chem.*, 2007, **17**, 3915; I. de Pedro, J. M. Rojo, J. L. Pizarro, J. Rodríguez Fernández, J. Sánchez-Marcos, M. I. Arriortua, T. Rojo, *J. Phys.: Condens. Matter*, 2006, **18**, 3767; J. M. Rojo, J. L. Mesa, L. Lezama, J. L. Pizarro, M. I. Arriortua, J. Rodríguez Fernández, G. E. Barberis, and T. Rojo, *Phys. Rev. B*, 2002, **66**, 094406.

64 E. S. Larrea, J. L. Mesa, J. L. Pizarro, R. Fernández de Luis, J. Rodríguez Fernández, T. Rojo, M. I. Arriortua, *Dalton Trans.*, 2012, **41**, 14170.

Three novel 3D open-framework fluorinated mixed valence Fe(II)-Fe(III) phosphites with channels templated by protonated tetramine chains were synthesized. The influence of the template as well as the partial substitution of Fe(II) by Co(II) on the resulting structures exhibiting interesting magnetic properties is discussed.